

Foreign object damage in a thermal barrier system: mechanisms and simulations

X. Chen^{b,*}, R. Wang^a, N. Yao^a, A.G. Evans^a, J.W. Hutchinson^b, R.W. Bruce^c

^a Princeton Materials Institute, Princeton University, Princeton, NJ 08540, USA

^b Division of Engineering and Applied Sciences, Harvard University, Cambridge, MA 02138, USA

^c GE Aircraft Engines, Cincinnati, OH 45215, USA

Received 11 January 2002; received in revised form 13 November 2002

Abstract

Experimental studies have been performed of foreign object damage (FOD) imparted to a thermal barrier system under conditions representative of those found in a turbine engine. The sub-surface damage has been characterized by using the focused ion beam (FIB) imaging system. The characterization reveals changes in the thermal barrier coating (TBC), caused by particle impact, that confirm and elaborate previous observations of FOD. These features include a permanent impression, a zone of densification, shear bands penetrating from the impact site to the interface with the bond coat, and delamination cracks extending away from the impact in the TBC adjacent to the interface. The dimensions of these features have been reported. A simulation procedure has been devised and implemented. The simulations have been performed in conjunction with a new non-dimensional analysis that allows the impact and material variables to be grouped into the smallest possible parameter set needed to characterize the stresses and projectile velocities, as well as the impression and densification zone dimensions. This parameterization provides explicit results for the stresses and displacements that arise as the projectile characteristics and material properties are varied over a range applicable to FOD in gas turbines. A scaling relation has been derived from the stress field and the penetration that relates the length of the interface delamination to the impact and material variables. A comparison of the simulations with the measurements indicates that the unknown impact velocity of the projectile can be ascertained from the penetration depth if the yield strength is known and vice versa. With this information, the scaling relation for the size of the interface delamination indicates consistency with the measured cracks. The implication is that delamination can be suppressed by lowering the high temperature hardness of the TBC and by increasing its toughness.

© 2002 Elsevier Science B.V. All rights reserved.

Keywords: Thermal barrier coating; Foreign object damage; Mechanism; Simulation

1. Introduction

Thermal barrier systems used in gas turbines exhibit several failure modes [1–13]. Prior assessments have focused primarily on modes governed by the energy density in the thermally grown oxide (TGO), which result in failure by either large-scale buckling or edge delamination [12]. Among the other modes, that based on foreign object damage (FOD) [14] is particularly important. The focus of this article is on the mechanisms leading to failure in the presence of such damage. The

study is in two parts. (i) An experimental assessment for a thermal barrier coating (TBC) comprised of yttria stabilized zirconia (YSZ), made by electron beam physical vapor deposition (EB-PVD) on a platinum–aluminide bond coat, impacted at high temperature by hard objects. (ii) A dynamic simulation of the response used to establish the penetration of the object into the TBC, as well as the extent and magnitude of the induced stresses. The two aspects are connected in an attempt to provide basic understanding of the mechanisms.

Prior studies have indicated that impact by small hard projectiles at high temperature can cause cracks to form near the impact site, which propagate through the TBC toward the interface with the TGO [14]. Visual evidence for oblique kink bands has also been presented,

* Corresponding author. Fax: +1-617-495-9837.

E-mail address: chen@esag.harvard.edu (X. Chen).

indicative of some plastic deformation occurring in the YSZ. The experiments and simulations performed in this study will provide additional characterization of the phenomena accompanying particle impact and establish preliminary scaling rules.

The experimental study is performed using an impact test protocol described elsewhere [14], which simulates the effects found in actual engine exposure. It consists of heating a cylindrical specimen of the type used for burner rig tests and subjecting to a flux of alumina particles. In some regions, the TBC spalls, exposing the TGO and/or the bond coat. The subsurface phenomena that precedes spalling have been investigated by using a focused ion beam (FIB) system to create cross-sections suitable for electron imaging. The FIB system permits sections to be created at a predetermined site within the damage zone, by using an ion beam that preserves the state of the material, and then allows cross-sectional imaging in a scanning electron mode.

The calculations are conducted by applying a method previously used to simulate particle impact in Ti alloys [15,16]. It uses the dynamic explicit finite element method (ABAQUS/Explicit) [17].

2. Materials, testing and characterization

Cylindrical specimens of Rene N5 nickel-based superalloy were used in this study. They were 89 mm long and 6.1 mm in diameter, with a 50 μm thick platinum–aluminide bond coat and a 7% YSZ TBC, 130 μm thick, made by EB-PVD. The specimens were mounted on a carousel in a burner rig [7] about 50 mm from the combustor exhaust, rotated at 500 rpm. The surface temperature of the TBC was controlled at 1232 $^{\circ}\text{C}$. A fixed quantity of alumina particulates was injected radially into the combustor. The particle size distribution was logarithmic normal, with the smallest being about 50 μm and the largest about 560 μm [14]. In transit, the particulates heat up and reach about 1450 $^{\circ}\text{C}$. They impact the specimen normal to the axis. The larger ones impact at about 10 ms^{-1} and often fragment during impact. The smaller ones impact at about 170 ms^{-1} . This laboratory test appears to simulate the damage found on airfoils in commercial engines [14]. The impact damage by the highest kinetic energy particulates is of primary interest here because they cause TBC delamination and spallation rather than gradual erosion. The impact damage occurs on the front and back of the specimens (Fig. 1). The latter happens because the particulates that bypass the first row of specimens accelerate through the center of the carousel and impact those furthest from the combustor. After the coating erodes by about 40 μm , the remaining TBC spalls in some regions, exposing the bond coat [14]. After testing, the damage on both the front and the back

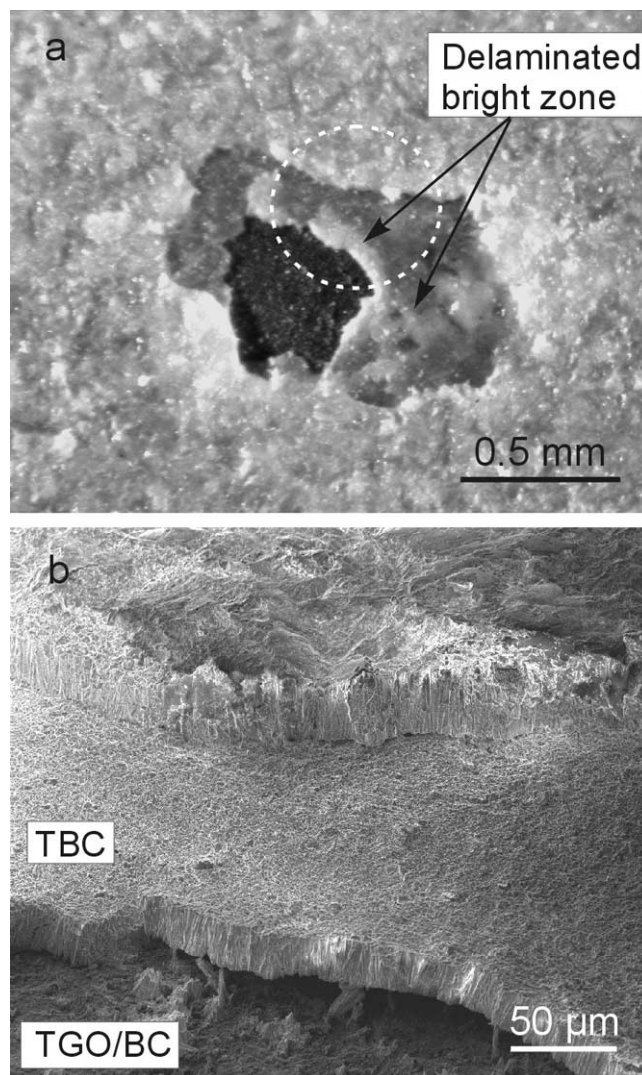


Fig. 1. Optical (a) and scanning electron (b) images showing the impact damage on the TBC. The delamination between the TBC and TGO/or bond coat (BC) extends to the surrounding area, giving rise to the bright contrast in (a). The right arrow in (a) shows a bright delamination zone where the FIB sections were performed.

of the samples was examined with an optical microscope (Leica MZ8, Wetzlar, Germany).

The thermal barrier material has a columnar grain structure and is porous [7]. The porosity is distributed at three different length scales [18]. To simplify the simulations, these details are neglected. They will be incorporated into future embellishments of the model. The YSZ is considered to be isotropic with an initial porosity in the range 10–20%, typical of that measured in actual systems [18].

The samples were coated with 6 nm carbon by ion sputtering deposition, then cross-sectioned and analyzed using a Dual-Beam Microscope (DB235, FEI Company, Hillsboro, Oregon). This instrument is equipped with a field emission electron microscope for high resolution imaging, and a FIB for sectioning at a pre-determined

site. For precision sectioning, a gallium ion beam is focused to 20 nm and bombards the surface at 30 kV. It targets a micro-area while operating in the SEM mode and creates a local cross-section in the FIB mode. The ion beam provides a relatively smooth surface, with minimal affect on the state of damage. Once sectioning has been completed, the section can be imaged in the SEM mode. This approach allows subsurface features created by the foreign object impact to be comprehensively characterized.

3. Observations

3.1. Plan views

Optical images of damage sites prior to sectioning with the FIB (Fig. 1a and b) indicate the scope of the spallation. The bright optical contrast beyond the central spall zone (Fig. 1a) indicates that the delamination extends into the surrounding TBC, consistent with the cross-sections described next. The higher resolution SEM images (Fig. 1b) indicate that the spall extends entirely within the oxide layers in a relatively planar manner. The crack usually propagates in the TBC, though occasionally oscillating between the thin TGO and the TBC. In the center of the spall, TBC hillocks still adhering to the bond coat are evident. For the specimen depicted on Fig. 1, a relatively large area around the central spall site had been eroded, leaving a TBC layer about half the thickness of the as-deposited coating. This is the region most amenable to the FIB studies addressed next.

3.2. Cross-sections

Images of several cross-sections through impact sites indicate the multiple effects schematically summarized on Fig. 2.

- i) Immediately beneath the impact site, the YSZ exhibits a densified zone, manifest as a region without electron contrast (Figs. 3 and 4b). The elimination of the contrast associated with the columnar grains and the disappearance of the porosity suggest that the densification occurs by plastic deformation, in accordance plasticity mechanisms [19]. Lateral cracks usually exist in the densified zone, and may extend to the surrounding area.
- ii) In some cases, a kink band emanates from the densification zone, at an inclination of about 45° (Fig. 4). The lower boundary of the band is cracked, reminiscent of similar bands found in aligned fiber composites under confined compression [20]. These cracks extend down to the interface with the TGO.

- iii) Upon reaching the interface, the cracks reorient into a delamination trajectory and extend up to several multiples of the remaining TBC thickness (Figs. 3 and 4). The cracks oscillate near the interface, mostly within the TBC, isolating hillocks of YSZ on the TGO side of the crack. The latter are associated with conical ‘pinched-off’ regions that form at impressions in the bond coat surface present before TBC deposition [9,11].

Since one of the impact sites analyzed has retained a portion of the alumina projectile (Fig. 3), which fragmented upon impact, some additional information can be elucidated. The depth and width of the residual impression (defined on Fig. 5) are, respectively, $\delta^R \approx 10 \mu\text{m}$ and $w^R \approx 30 \mu\text{m}$. The diameter of the impacting particle is estimated from the radius of curvature of the entrained particle (Fig. 3) to be, $D \approx 100 \mu\text{m}$. The radius of the densified zone in the vertical direction is of order, $R_{Dv}^R \approx 60 \mu\text{m}$. The delamination cracks extend beyond the field of view in Figs. 3 and 4. Lower magnification images indicate that their total length is in the range, $2a \approx 150 \mu\text{m}$. These characteristic dimensions are used below in the comparison with the numerical simulations.

4. Simulations

4.1. Dimensional analysis

In general, for impact problems, the independent input variables include the coordinate vector \mathbf{x} (with components x_i ($i = 1-3$)), the friction coefficient μ , the projectile diameter D , its initial impact velocity v_0 and its density ρ_p . For a TBC layer on a substrate, the additional input parameters include its initial porosity, f_0 , thickness h_{tbc} , Young’s modulus, E_{tbc} , yield strength and strain σ_{tbc}^Y and, $\varepsilon_{\text{tbc}}^Y = \sigma_{\text{tbc}}^Y/E_{\text{tbc}}$ and density, ρ_{tbc} . The relevant bond coat properties are $\varepsilon_{\text{bc}}^Y$, E_{bc} , ρ_{bc} and thickness h_{bc} . The choice of Poisson’s ratio has little influence and will be taken as $\nu = 0.25$ for all constituents. All output variables of interest are functions of time t . They include the impression depth, δ , crater diameter, w , plastic pile-up height, δ_p , the projectile speed v , the ricochet velocity v^R , and the stresses σ_{ij} .

Provided that the impact crater does not penetrate to the TBC/bond coat interface, the properties of the bond coat and substrate are relatively unimportant. The kinetic energy of an incoming spherical particle is, $U = (\pi/12)\rho_p D^3 v_0^2$. From dimensional analysis, the dimensionless stress history in the TBC is:

$$\frac{\sigma_{ij}(\mathbf{x}, t)}{\sigma_{\text{tbc}}^Y} = F_{ij} \left[\frac{\mathbf{x}}{D}, \frac{t \sqrt{\sigma_{\text{tbc}}^Y / \rho_p}}{D}, f_0, \frac{U}{\sigma_{\text{tbc}}^Y D^3}, \frac{D}{h_{\text{tbc}}}, \varepsilon_{\text{tbc}}^Y, \frac{\rho_p}{\rho_{\text{tbc}}} \right] \quad (1)$$

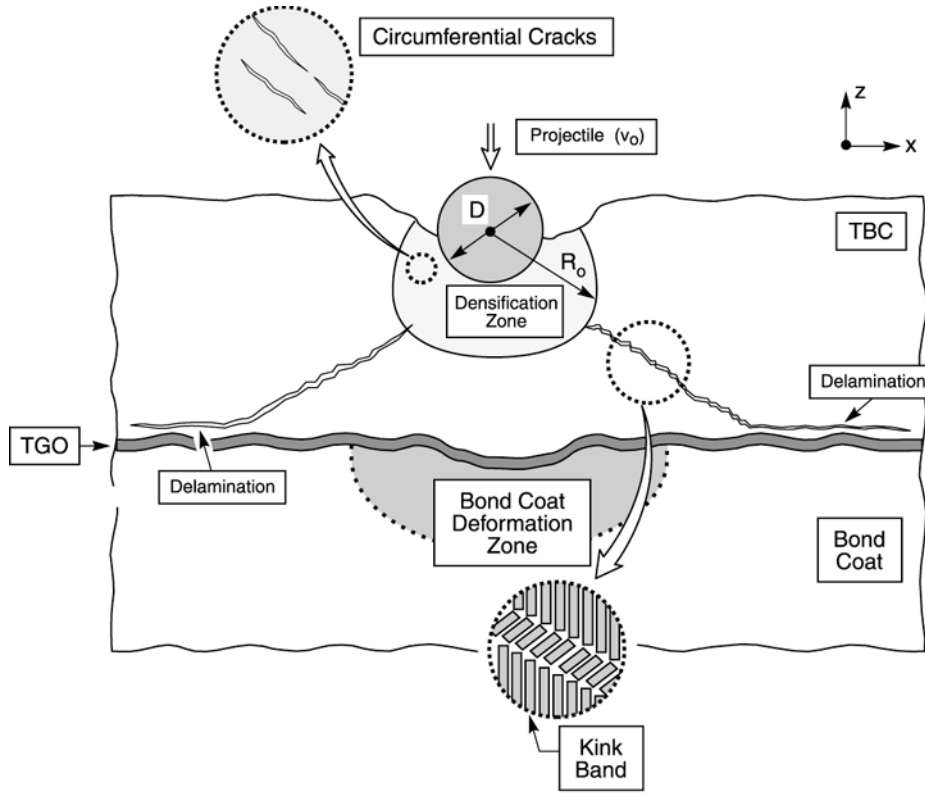


Fig. 2. Schematic illustrating the different impact zones.

The normalized size of the densification zone, $R_D(t)/D$, the normalized penetration depth, $\delta(t)/D$, the dimensionless pile-up, $\delta_p(t)/D$, the dimensionless contact diameter, $w(t)/D$, as well as the normalized foreign object speed $v(t)/v_0$ are functions of the same variable set, $t\sqrt{\sigma_{\text{tbc}}^Y/\rho_p}/D$, f_0 , $U/(\sigma_{\text{tbc}}^Y D^3)$, $\varepsilon_{\text{tbc}}^Y$, ρ_p/ρ_{tbc} , and D/h_{tbc} . While many parameters characterize the problem, dimensional analysis allows the set to be narrowed.

Finite plastic deformation and strains are involved in the impact process. Recent studies of static indentation and of dynamic impact of homogeneous materials [15] have indicated that, whenever the plastic deformations appreciably exceed those caused by elastic (Hertzian) contact, the geometric output variables (such as δ , δ_p and w), as well as the residual stresses, when properly normalized, are independent of the elastic modulus.

For a homogeneous substrate with yield strength σ_s^Y and density ρ_s , Chen and Hutchinson [15] have shown that the normalized impact energy, $\Omega^* = KE/(\sigma_s^Y D^3) \equiv (\pi/12)(\rho_p/\sigma_s^Y)v_0^2$, plays a role similar to the normalized work done by a spherical indenter, leading to dimensionless relations nearly independent of $\varepsilon_s^Y = \sigma_s^Y/E_s$ and the particle-substrate density ratio, ρ_p/ρ_s . Note that the quantity $\sqrt{\sigma_s^Y/\rho_p}$ has dimension of velocity and $D/\sqrt{\sigma_s^Y/\rho_p}$ has dimension of time. The dimensionless

time variable $t\sqrt{\sigma_s^Y/\rho_p}/D$ scales the transient remarkably well [15].

Inspired by the above observations for a cylinder, diameter D , with kinetic energy/length U , it is convenient to define dimensionless quantities for plane strain TBC impact as:

$$\Omega \equiv \frac{U}{(\sigma_{\text{tbc}}^Y D^2)} = \left(\frac{\pi}{8}\right) \left(\frac{\rho_p}{\sigma_{\text{tbc}}^Y}\right) v_0^2 \quad (2a)$$

and

$$\bar{t} \equiv \frac{t\sqrt{\sigma_{\text{tbc}}^Y/\rho_p}}{D}, \quad (2b)$$

The inference that the stress history and the geometric output variables would be essentially independent of $\varepsilon_{\text{tbc}}^Y$ and ρ_p/ρ_{tbc} is verified in the next section. It will also be affirmed that the parameter D/h_{tbc} has a secondary role when the maximum penetration is considerably less than the TBC thickness. Consequently, the primary dependency of the stresses in thick TBC layer (where $\delta^{\text{max}}/D < 1/2$) is:

$$\frac{\sigma_{ij}(\mathbf{x}, t)}{\sigma_{\text{tbc}}^Y} = F_{ij} \left[\frac{\mathbf{x}}{D}, \frac{t\sqrt{\sigma_{\text{tbc}}^Y/\rho_p}}{D}, \Omega, f_0 \right], \quad (3a)$$

and the residual stresses are:

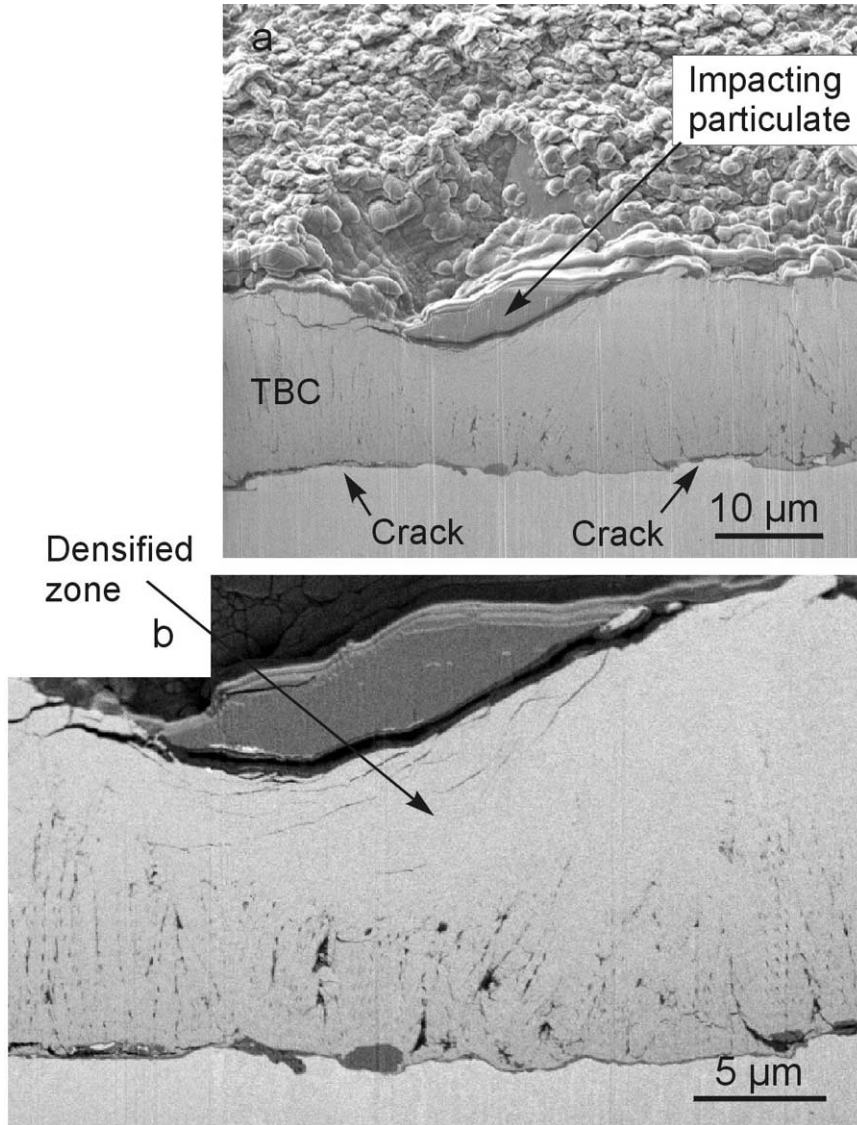


Fig. 3. FIB cross-section reveals the impact damage by an individual particulate still embedded in the TBC. A densified zone forms immediately underneath the impact site. Circumferential cracks are evident inside the densified zone, as well as near the boundary between the TBC and the TGO layer. (a) Secondary electron image; (b) Back scatter electron image. The section plane is 38° to the electron beam.

$$\frac{\sigma_{ij}^R(x)}{\sigma_{tbc}^Y} = F_{ij} \left[\frac{x}{D}, \Omega, f_0 \right] \quad (3b)$$

The residual geometric parameters characterizing FOD, R_D^R/D , δ^R/D , δ_P^R/D , and w^R/D , have primary dependence only on f_0 and Ω : a remarkable collapse of the large parameter set to only two quantities.

The ricochet velocity, v^R , scales more naturally with the elastic wave speed of the substrate, and for this purpose introduce $v_{tbc} \equiv \sqrt{E_{tbc}/\rho_{tbc}}$, such that the normalized velocity, v^R/v_0 , depends on ε_{tbc}^Y and ρ_P/ρ_{tbc} , as well as f_0 and Ω .

4.2. The finite element method

With the above assessment providing scaling guidelines, numerical simulations have been used to determine the dimensionless functional forms. The transient stress fields are calculated with the finite element method, by using the ABAQUS/Explicit code, based on the explicit time integration method [17]. The term ‘explicit’ designates that the state at the end of the increment is based solely on the displacements, velocities, and accelerations at the beginning of the increment. Therefore, the time increments are necessarily a small fraction of the time for an elastic wave to traverse the smallest element (on

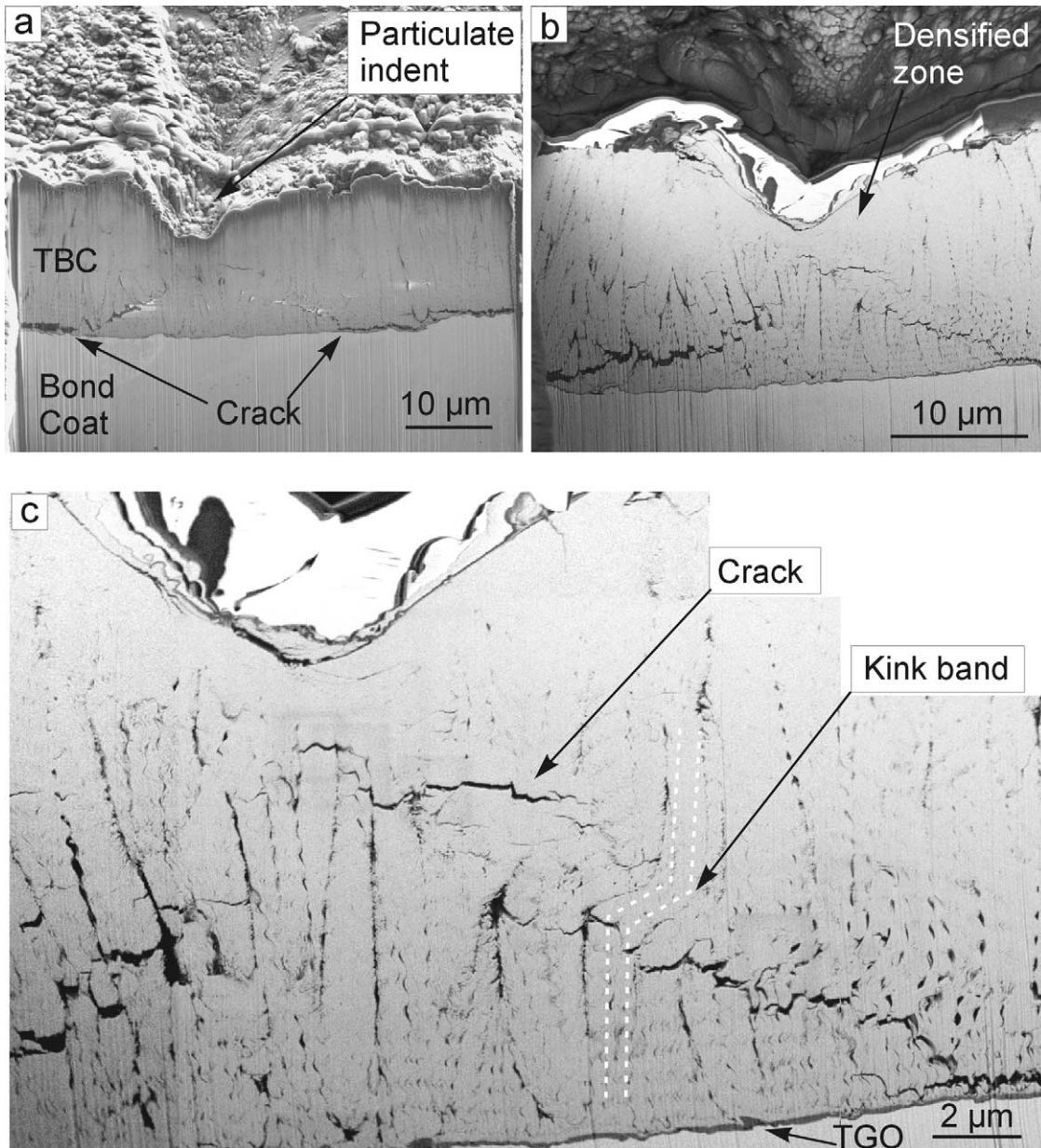


Fig. 4. FIB cross-section showing the kink band in the TBC beneath the impact site. Cracks extend along the kink band from the densified zone to the TGO layer. (a) SE image; (b) BSE image of the same site, the top bright layer is the platinum protective coating deposited under the microscope; (c) BSE image of the kink band (marked by dashed lines) and cracks. Section plane is 38° to the electron beam.

the order of 10^{-3} ns in the present analysis) and a very small fraction of D/v_{tbc} . It is assumed that the particles remain intact (do not fragment). It is believed that the fragmentation that occurs in practice happens after the penetration phase of the impact is complete, indicative of a second order effect on the response of the TBC.

To make connection with the experiments involving elongated particles, plane-strain deformation is assumed with $\mathbf{x} = (x_1, x_2)$. The rigid contact surface option simulates a cylindrical particle with diameter D , and the option for finite deformation and strain is employed.

The size of the layered system is taken to be sufficiently large compared with the final impact crater such that it may be considered infinite in x_1 , and semi-infinite in x_2 . A typical mesh for the 2D impact problem comprises more than 54 000, four-node elements (with reduced integration). All of the materials (the superalloy, bond coat, and TBC) are taken to be elastic-perfectly plastic, with a Von Mises yield surface. The inertia and the wave effects are all included in the explicit analysis. Coulomb friction is invoked in the calculations, where the friction coefficient is taken to be 0.1 (almost frictionless). This

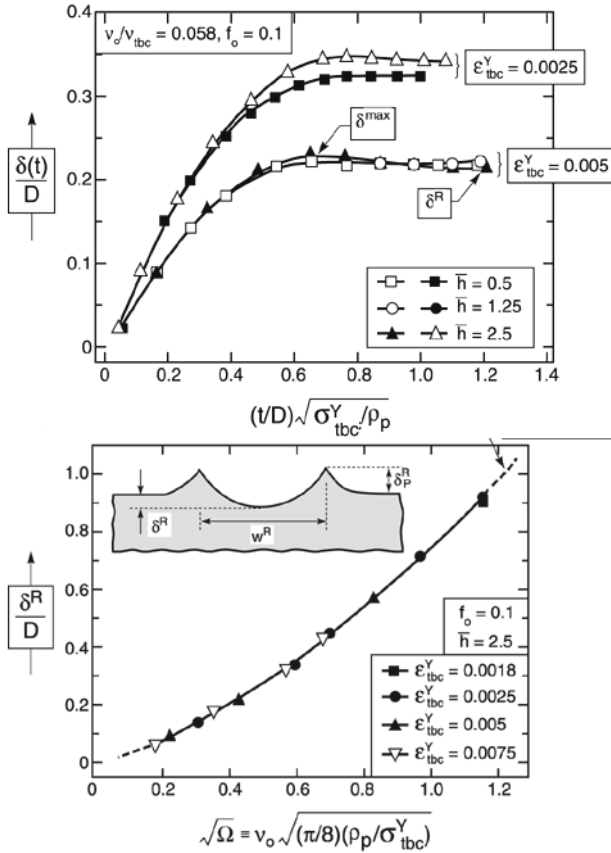


Fig. 5. (a) Variation of the normalized indentation depth δ/D with normalized time $t\sqrt{\sigma_{tbc}^Y/\rho_p}/D$, as a function of TBC yield strain ϵ_{tbc}^Y and normalized TBC thickness $\bar{h} = h_{tbc}/D$, where $f_0 = 0.1$ and $v_0/v_{tbc} = 0.058$. The results are insensitive to \bar{h} . (b) The residual indent depth δ^R/D is independent of ϵ_{tbc}^Y and only a function of $\sqrt{\Omega}$ at $f_0 = 0.1$.

value has been previously used in the study of impact on Ti alloys, providing good agreement with experiments [16].

4.3. Results

A series of simulations has been performed by varying the dimensionless impact energy, $\Omega = U/(\sigma_{tbc}^Y D^2)$, the TBC thickness, $\bar{h} = h_{tbc}/D$, and the TBC yield strain, ϵ_{tbc}^Y . While the results will be presented in dimensionless terms, the specific dimensional ranges are pertinent to the interpretation. The foreign object is modeled in plane strain with diameter $D = 20 \mu\text{m}$, for a series of impact velocities ranging from 25 to 300 m s^{-1} . The cylinder has the density of alumina, $\rho_p = 4000 \text{ kg m}^{-3}$, but otherwise is rigid. The mechanical properties of the superalloy substrate play a minor role: they have been taken to be representative of Ni alloys. The thickness of bond coat is 50 μm , with a Young's modulus of 200 GPa and yield strength of 60 MPa. The TBC is taken to be isotropic. The effects of the anisotropy caused by the columnar structure will be introduced in a follow-on

Table 1
Estimate of relevant properties of TBC at 1200 °C

Yield strength [20], σ_{tbc}^Y	150 MPa
Modulus, E_{tbc} [7,11]	40 GPa
Yield strain	4×10^{-3}
Toughness [7]	20 J m^{-2}

study. All the parameters are chosen to encompass the range expected at an operating temperature of about 1200 °C (Table 1). The Gurson constitutive model [19] for porous materials is invoked as a characterization, enabling the simulation of densification. A representative initial void volume fraction of $f_0 = 0.1$ is prescribed [18]. The Young's modulus is 40 GPa and the high temperature yield strength varied between 70 and 300 MPa. The thickness is varied between 10 and 50 μm and its density at $f_0 = 0$ is 5900 kg m^{-3} .

The results of the simulations are summarized on Figs. 5–9. The salient trends and representative residual formulae are elaborated.

- i) The normalized penetration $\delta(t)/D$ is insensitive to TBC thickness as long as $\delta^R < h_{tbc}$ (Fig. 5a). The residual penetration, δ^R , is slightly smaller than the

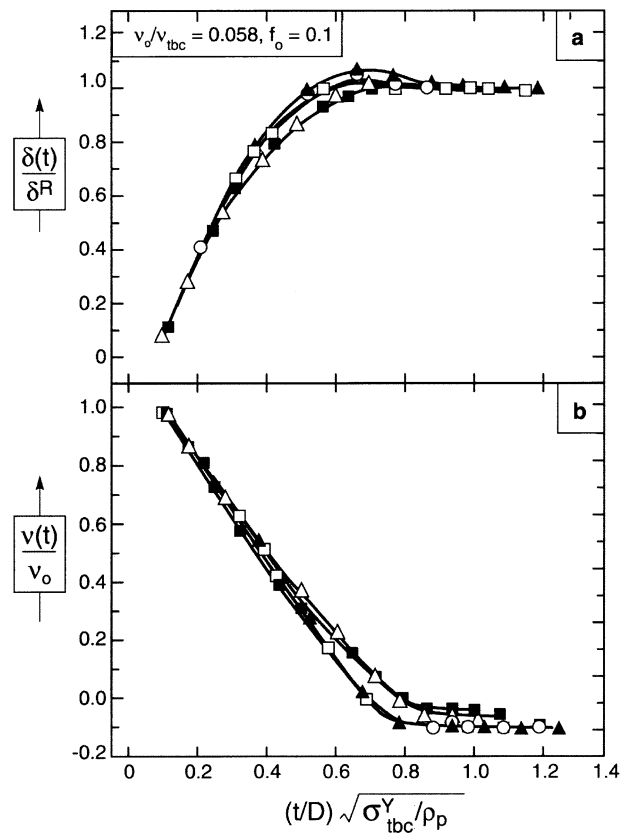


Fig. 6. (a) Normalized indented depth history $\delta(t)/\delta^R$ is essentially independent of ϵ_{tbc}^Y except at the peak penetration just at the beginning of rebound. (b) The time history of the particle velocity $v(t)/v_0$ is insensitive to \bar{h} but varying with ϵ_{tbc}^Y .

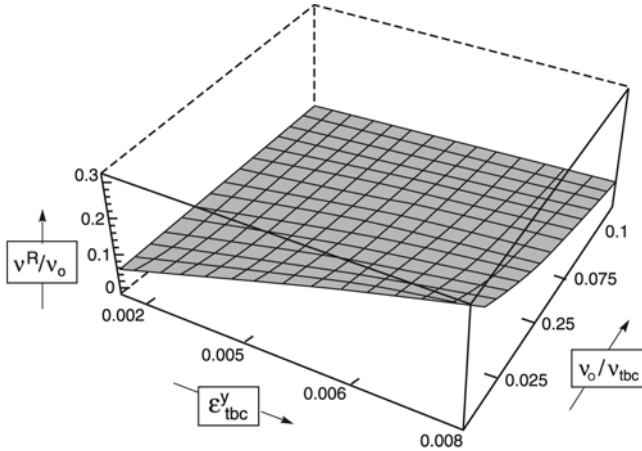


Fig. 7. Three-dimensional plot of the functional form in (5), where the Ricochet velocity v^R/v_0 is varying with $\varepsilon_{\text{tbc}}^Y$ and v_0/v_{tbc} .

maximum, δ^{max} , because of elastic spring-back. Moreover, the choice of dimensionless time, $t \sqrt{\sigma_{\text{tbc}}^Y/\rho_p}/D$, scales the transient very successfully. That is, the residual penetration depends only on Ω and f_0 , except at very low ratios of ρ_p/ρ_{tbc} [15]. Over the present parameter range, restricted to $f_0 = 0.1$ (Fig. 5b):

$$\bar{\delta}^R \equiv \frac{\delta^R}{D} \approx 0.38 \sqrt{\Omega}(1 + 0.84 \sqrt{\Omega}) \quad (4)$$

These calculations, when re-plotted as $\delta(t)/\delta^R$ (Fig. 6a) emphasize the insensitivity to $\varepsilon_{\text{tbc}}^Y$, except at the beginning of rebound (since the spring-back is elastic).

- ii) The time history of the particle velocity, $v(t)/v_0$, prior to rebound is nearly independent of $\varepsilon_{\text{tbc}}^Y$ (Fig. 6b). The ricochet velocity, v^R/v_0 , depends on the TBC modulus (through $\varepsilon_{\text{tbc}}^Y$). A function that fits over the present parameter range, with $\rho_p/\rho_{\text{tbc}} = 0.68$, is (Fig. 7)

$$\frac{v^R}{v_0} \approx -58\varepsilon_{\text{tbc}}^Y \left(1 - 2.1 \sqrt{\frac{v_0}{v_{\text{tbc}}}} - 17\varepsilon_{\text{tbc}}^Y \right) \quad (5)$$

with $v_{\text{tbc}} = \sqrt{E_{\text{tbc}}/\rho_{\text{tbc}}}$.

- iii) The residual plastic pile-up height δ_P^R is independent of the TBC stiffness and takes the form ($f_0 = 0.1$)

$$\bar{\delta}_P^R \equiv \frac{\delta_P^R}{D} \approx 0.011 \sqrt{\Omega}(1 + 3.1 \sqrt{\Omega} + 27\Omega). \quad (6)$$

- iv) The residual impression width w^R can be expressed in terms of the residual penetration and pile-up from simple geometric analysis:

$$\begin{aligned} \bar{w}^R &\equiv \frac{w^R}{D} \\ &= 2 \sqrt{\bar{\delta}^R + \bar{\delta}_P^R - (\bar{\delta}^R + \bar{\delta}_P^R)^2} \quad \text{when } \delta^R + \delta_P^R \\ &< \frac{D}{2} \end{aligned} \quad (7)$$

with $w^R \approx D$ when $\delta^R + \delta_P^R > D/2$. In Eqs. (4)–(7), the fitting functions are chosen such that they are consistent with the following general requirements: $\bar{\delta}^R$, $\bar{\delta}_P^R$, $\bar{w}^R \rightarrow 0$ when $\Omega \rightarrow 0$, and $v^R/v_0 \rightarrow 0$ when $\varepsilon_{\text{tbc}}^Y \rightarrow 0$.

Contours of the void volume fraction (Fig. 8a), normal stress, $\sigma_{22}/\sigma_{\text{tbc}}^Y$ (Fig. 8b), and shear stress $\sigma_{12}/\sigma_{\text{tbc}}^Y$ (Fig. 8c) in a thick TBC layer ($\bar{h} = 2.5$) are summarized at five representative stages of impact (with $f_0 = 0.1$ and $\Omega = 0.35$). The stress histories probe the temporal function in (Eq. 3a). The residual stress (Eq. 3b) and porosity were obtained at $\bar{t} > 3$. Note that the results are essentially independent of $\varepsilon_{\text{tbc}}^Y$, ρ_p/ρ_{tbc} , and are invariant with \bar{h} (when $\bar{h} > 1$).

The densification zone, defined as the region where the gradient of void volume fraction is non-zero, spreads as the penetration increases. Its shape can be approximated by an ellipse (Fig. 8a) with major axis R_{Dv} (vertical direction) and minor axis R_{Dh} (horizontal direction). Over present parameter range the residual quantities scale with w^R , whereupon at sufficiently large TBC thickness:

$$\begin{aligned} \frac{R_{Dv}^R}{w^R} &\approx 2.0 + \frac{\delta^R}{w^R} \\ \frac{R_{Dh}^R}{w^R} &\approx 0.37 + 1.8 \sqrt[4]{\Omega} \end{aligned} \quad (8)$$

The stresses of most interest to TBC failure are the normal stress perpendicular to the interface, σ_{22} , which governs delamination, and the shear stress σ_{12} , which determine shear banding. During penetration, a confined zone of normal compression develops, coincident with the densification zone. The associated displacements cause the TBC just outside this zone to form a domain of intense shear (Fig. 8c), with magnitude about half the yield strength. The prominent shear region expands as the projectile penetrates until the particle begins to rebound (at $\bar{t} = t \sqrt{\sigma_{\text{tbc}}^Y/\rho_p}/D = 0.8$ in Fig. 8). This is the phenomenon that activates kink bands, discussed below. The shear stress drops immediately after spring-back, and the residual $\sigma_{12}/\sigma_{\text{tbc}}^Y$ is less than half its peak.

Once penetration is complete, interactions with the bond coat cause the normal stress to become tensile, both within the TBC and along the interface (Fig. 8).

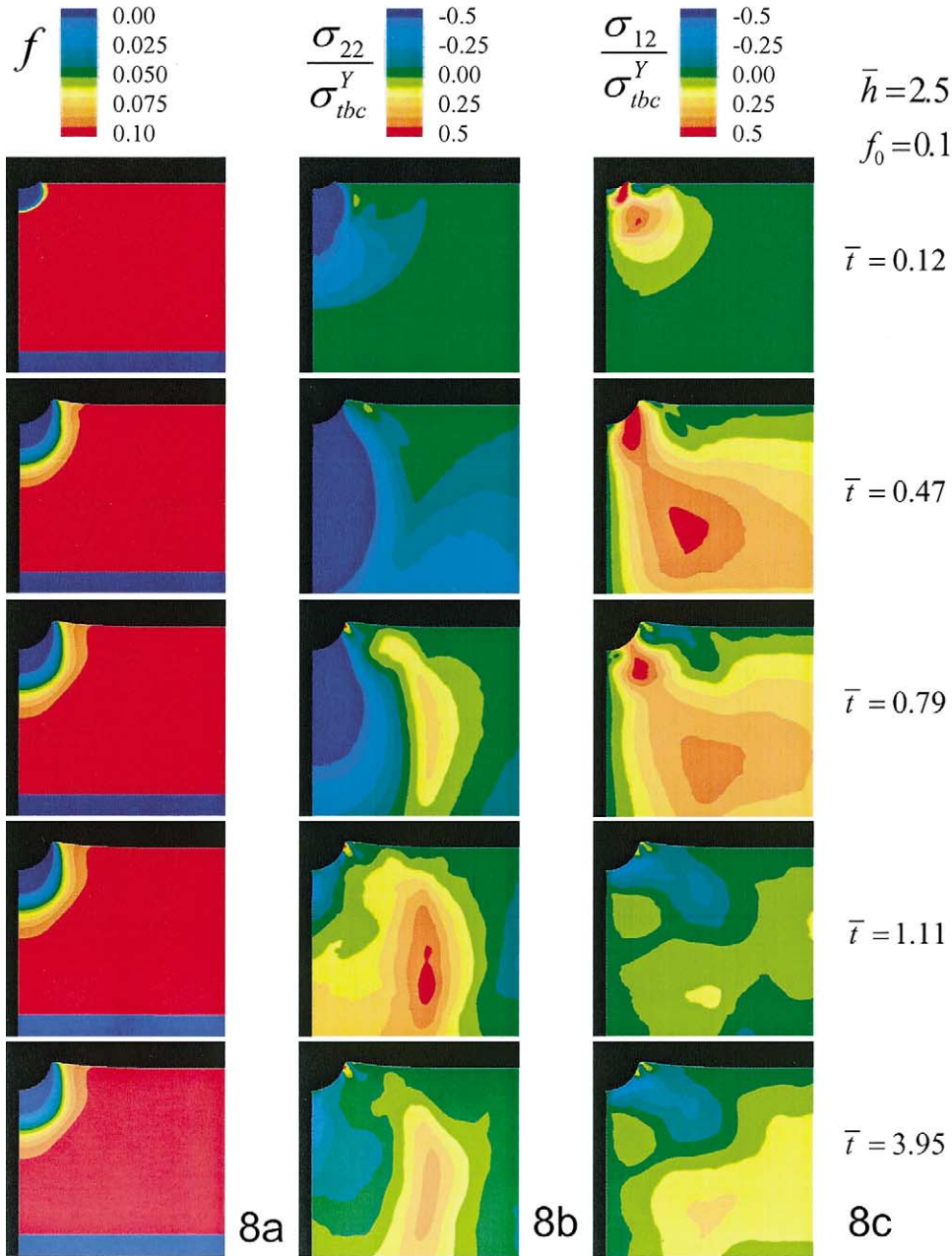


Fig. 8. Contours of constant values of (a) the void volume fraction f , (b) normal stress component $\sigma_{22}/\sigma_{tbc}^Y$, and (c) shear stress component $\sigma_{12}/\sigma_{tbc}^Y$. The TBC layer has a thickness of $\bar{h} = 2.5$ and a initial porosity of $f_0 = 0.1$. Five representative instants in the impact history are shown with $\bar{t} = t\sqrt{\sigma_{tbc}^Y/\rho_p}/D = 0.12, 0.47, 0.79, 1.11$ and 3.95 .

For the conditions used to perform the calculations, the maximum principal tension approaches $0.6\sigma_{tbc}^Y$ (Fig. 8b). Some normal tension is retained after the impact, resulting in a residual stress $\sigma_{22}^R \approx 0.4\sigma_{tbc}^Y$. This is the stress that activates delamination at the interface and the spallation in TBC, discussed below. For a thick TBC layer ($\bar{h} = 2.5$), while the maximum and residual normal stresses increase as the impact energy increases (Fig. 9), the former is quite insensitive to Ω . The largest values at the highest energy, $\Omega = 1.4$, are: $\sigma_{22}^{\max} \rightarrow 0.75\sigma_{tbc}^Y$, and $\sigma_{22}^R \approx 0.5\sigma_{tbc}^Y$. Note that the maximum normal stress

does not necessarily occur at the interface. At low impact energies ($\sqrt{\Omega} < 0.15$) it occurs within the TBC.

The maximum and residual normal stresses are found to decrease at smaller TBC thickness, when $\bar{h} < 1$, because of the reduced strain energy stored in the thinner TBC as the projectile penetrates.

4.4. Interface delamination

The impact creates a residual tensile stress along the interface on both sides of the crater (Fig. 8). The scaling

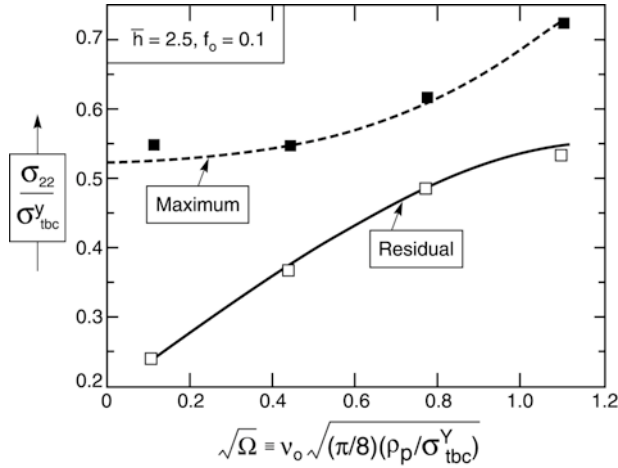


Fig. 9. Plot of the peak and residual normal stress at the interface, as a function of the normalized impact velocity.

that governs the driving force for the interface delamination induced by this stress is derived by analogy with the formation of lateral cracks in homogeneous ceramics upon elastic–plastic indentation [21,22]. The penetration is approximated by the elastic–perfectly plastic solution for axi-symmetric expansion of a cylindrical void in an infinite solid in plane strain. A sketch motivating the approximation is included in Fig. 10. The material properties are taken to be those of the TBC (Table 1). Upon assuming that the radius of the plastic zone is larger than h_{tbc} , the radial stress at a distance h_{tbc} from the center of the void becomes:

$$\sigma_{\text{rr}} = -\frac{\sigma_{\text{tbc}}^{\text{Y}}}{2} \left[1 + \ln \left(\frac{2}{3\pi} \frac{E_{\text{tbc}}}{\sigma_{\text{tbc}}^{\text{Y}}} \frac{\Delta A}{\pi h_{\text{tbc}}^2} \right) \right] \quad (9)$$

where ΔA is the area expansion of the void. Upon applying Eq. (9) to the half-space, $\Delta A/2$ will be identified with the cross-sectional area of the impact crater. The formula neglects the small stress change upon elastic unloading.

The stress in Eq. (9) is used to approximate the compression on the interface directly below the impact crater (Fig. 8), resulting in a compressive force (per unit depth), $P \sim \sigma_{\text{rr}} h_{\text{tbc}}$. Since the force is zero, the tensile stresses on either side scale in the same manner. A crack of dimension a on the interface (Fig. 10) experiences a stress intensity factor, $K \sim P/\sqrt{a}$ [23]. The associated energy release rate scales as $G = K^2/E_{\text{tbc}}$ or

$$\frac{GE_{\text{tbc}}a}{(\sigma_{\text{tbc}}^{\text{Y}} h_{\text{tbc}})^2} \sim \frac{1}{4} \left[1 + \ln \left(\frac{2}{3\pi} \frac{E_{\text{tbc}}}{\sigma_{\text{tbc}}^{\text{Y}}} \frac{\Delta A}{\pi h_{\text{tbc}}^2} \right) \right]^2 \quad (10)$$

with ΔA twice the area of the impact crater. Equating G to the TBC toughness, Γ_{tbc} converts Eq. (10) into a scaling relation for the length, a , of the interface delamination. Upon using Eq. (4) and Eq. (7) to express $\Delta A/D^2$ directly in terms of Ω , a plot of the non-dimensional delamination length is presented on Fig. 10 for two $\epsilon_{\text{tbc}}^{\text{Y}}$ (with $D/h_{\text{tbc}} = 0.4$, the experimental condition). This figure provides a direct association between the extent of delamination, the material properties and the system dimensions.

A similar analysis for spherical particles based on the solution for the spherically symmetric expansion of a void in an infinite solid gives:

$$\frac{GE_{\text{tbc}}a^3}{(\sigma_{\text{tbc}}^{\text{Y}} h_{\text{tbc}}^2)^2} \sim \frac{4}{9} \left[1 + \ln \left(\frac{1}{2\pi} \frac{E_{\text{tbc}}}{\sigma_{\text{tbc}}^{\text{Y}}} \frac{\Delta V}{h_{\text{tbc}}^3} \right) \right]^2 \quad (11)$$

with ΔV twice the volume of the impact crater.

Finally, we note that, upon impact by smaller projectiles, the cracks may be confined to the TBC, resulting in erosion. Then, the TBC thickness is no longer the relevant length scale and the crack extent should be similar to that for lateral cracks in a homogeneous medium [22].

5. Comparison with measurements

A comparison between the measurements and simulations is performed in the following manner. (a) The yield strength of the TBC is obtained from high temperature compression measurements [24] as, $\sigma_{\text{tbc}}^{\text{Y}} \approx 150$ MPa (Table 1). (b) Since the specific impact velocity is unknown, the measured impression depth provides an estimate. The size of the densified zone provides a consistency check. (c) Once this has been accomplished,

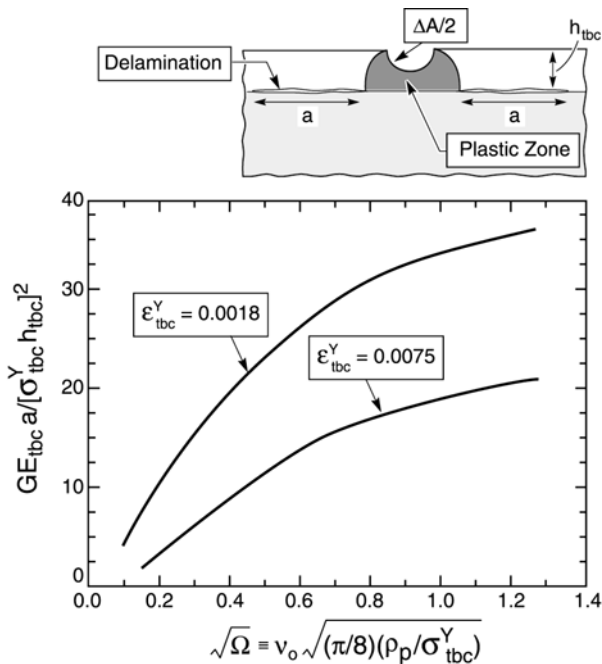


Fig. 10. The variation in the non-dimensional delamination length with normalized impact velocity for two choices of the TBC yield strain, with λ a scaling coefficient of order unity.

the stresses may be estimated and used with a mechanics analysis to rationalize delamination and shear banding.

Impressions in the measured size range ($\delta^R = 10 \mu\text{m}$ and $D = 100 \mu\text{m}$, Figs. 3 and 4), correspond to small Ω , whereupon Eq. (4) reduces to, $\delta^R/D \approx 0.38 \sqrt{\Omega}$. Inserting δ^R and D into Eq. (4), with Eqs. (2a) and (2b) used as the definition of Ω , and upon using $\sigma_{\text{tbc}}^Y \approx 150 \text{ MPa}$, an explicit estimate of the impact velocity is obtained as, $v_0 \approx 25 \text{ m s}^{-1}$. This is within the range ascertained experimentally [14]. The corresponding value of the non-dimensional velocity is, $\Omega \approx 0.06$. At this Ω , the simulations indicate a maximum tensile stress located at the interface, rather than internal to the TBC, rationalizing the observations (Figs. 3 and 4) and allowing the following assessment of interface delamination. The largest dynamic tensile stresses are about 90 MPa and the residual stresses about 45 MPa.

Based on the preceding estimate, $\sqrt{\Omega} \approx 0.25$, with $\varepsilon_{\text{tbc}}^Y \approx 4 \times 10^{-3}$ and TBC toughness $\Gamma_{\text{tbc}} \approx 20 \text{ J mm}^{-2}$ (Table 1), Fig. 10 may be used to estimate the size of the interface delamination caused by the impact (Fig. 3) as, $a \approx 50 \mu\text{m}$: somewhat smaller than the measured size ($a \approx 75 \mu\text{m}$). Given the simplifications used to obtain Eq. (10), this correspondence provides credence in the scaling behavior. From a practical perspective, the important implication is that the extent of delamination diminishes upon lowering the high temperature yield strength of the TBC and upon elevating its toughness. There are also strong effects of projectile velocity and density embedded in the trend in Ω .

The densification zone radius may be determined directly from Eq. (8), as $R_{\text{Dv}}^R \equiv 2.3w^R \approx 70 \mu\text{m}$. It is slightly larger than the measured zone size, $R_{\text{Dv}}^R \approx 60 \mu\text{m}$.

6. Implications and conclusions

A capability for measuring the sub-surface features associated with impact of TBCs by foreign objects has been demonstrated, as well as an approach for the full dynamic simulation of the displacements and stresses induced by the impact. The simulations have been conducted within a range of particle size and velocity that typify gas turbine operation and have incorporated best estimates of the properties of the TBC at elevated temperature. The properties include an initial porosity, with consequent densification in the immediate vicinity of the impact site.

A comparison between the simulations and measurements has been conducted in the following manner. The measured crater size and particle diameter, as well as a TBC yield strength assessed from the hardness (at 1200 °C), have been used with the simulations to estimate the unknown impact velocity. The estimate is

within the range expected from the experimental protocol. Based on this velocity, the maximum stresses have been estimated, as well as the size of delamination at the interface caused by the residual tensile stress. Given the simplifications used to assess the extent of cracking, the delamination sizes are deemed sufficiently close to the measurements to lend credence to the scaling inferences.

The principal implication is that the extent of delamination could be substantially reduced by lowering the high temperature hardness of the TBC material and also decreased by increasing its toughness. Moreover, there are strong influences of particle velocity, density and diameter that might permit definition of a threshold below which delamination can be averted. This remains to be established.

References

- [1] R.A. Miller, *Journal of the American Ceramic Society* 67 (1984) 517.
- [2] J.T. DeMasi-Marcin, D.K. Gupta, *Surface Coating Technology* 68/69 (1994) 201.
- [3] NRC report, R. Hillery (Ed.), *Coatings For High Temperature Structural Materials*, National Academy Press, 1996.
- [4] S.R. Choi, D. Zhu, R.A. Miller, *Ceramic Engineering and Science* 19 (1998) 293.
- [5] M.J. Stiger, N.M. Yanar, M.G. Topping, F.S. Pettit, G.H. Meier, *Zeitschrift fur Metallk* 90 (1999) 1069.
- [6] P.K. Wright, A.G. Evans, *Current Opinion in Solid State and Materials Science* 4 (1999) 255.
- [7] A.G. Evans, D.R. Mumm, J.W. Hutchinson, G.H. Meier, F.S. Pettit, *Progress in Materials Science* 46 (2001) 505.
- [8] M. Gell, K. Vaidyanathan, B. Barber, J. Cheng, E. Jordan, *Metallurgical and Materials Transaction* 30A (1999) 427.
- [9] D.R. Mumm, A.G. Evans, I. Spitsberg, *Acta Materialia* 49 (2001) 2329.
- [10] V. Tolpygo, D.R. Clarke, *Acta Materialia* 48 (2000) 3283.
- [11] J.A. Ruud, A. Bartz, M.P. Borom, C.A. Johnson, *Journal of the American Ceramic Society* 84 (2001) 1545.
- [12] S.R. Choi, J.W. Hutchinson, A.G. Evans, *Mechanics of Materials* 31 (1999) 431.
- [13] I. Spitsberg, D.R. Mumm, A.G. Evans, *Acta Materialia*, in press.
- [14] R.W. Bruce, *Tribology Transactions* 41 (1998) 399.
- [15] X. Chen, J.W. Hutchinson, *Journal of the Mechanics and Physics of Solids* 50 (2002) 2669.
- [16] B.L. Boyce, X. Chen, J.W. Hutchinson, R.O. Ritchie, *Mechanics of Materials* 33 (2001) 441.
- [17] ABAQUS version 5.8 User's Manual. Hibbit, Karlsson & Sorensen Inc., Pawtucket, RI, 1999.
- [18] T.J. Lu, C. Levi, H.N.G. Wadley, A.G. Evans, *Journal of the American Ceramic Society* 84 (2001) 2937–2946.
- [19] A.L. Gurson, *Journal of Engineering Materials and Technology* 99 (1977) 2.
- [20] B. Budiansky, N.A. Fleck, *Journal of the Mechanics and Physics of Solids* 41 (1993) 183.
- [21] R.F. Cook, G.M. Pharr, *Journal of the American Ceramic Society* 73 (1990) 787.
- [22] D.B. Marshall, B.R. Lawn, A.G. Evans, *Journal of the American Ceramic Society* 65 (1982) 561.
- [23] H. Tada, P. Paris, G. Irwin, *Handbook of Stress Intensity Factors*, Del Research, 1985.
- [24] M. Watanabe, A.G. Evans, unpublished research.